DOI: 10.1002/chem.200600155

Synthesis and Characterization of Mixed-Valent Manganese Phosphonate Cage Complexes

Maheswaran Shanmugam,[a] Guillaume Chastanet,[b] Talal Mallah,[c] Roberta Sessoli,[b] Simon J. Teat,[d] Grigore A. Timco,[a] and Richard E. P. Winpenny*[a]

Abstract: The reaction of phenylphosphonic acid ($PhPO_3H_2$) with the mixed-valent basic oxo-centered manganese triangle $[Mn_3O(O_2CCMe_3)_6(py)_3]$ (**1**; where py = pyridine) in the presence of a suitable base gives four different manganese clusters depending on the identity of the base. The syntheses and structural characterization of $[Mn_{18}(\mu_3\text{-}O)_8(PhPO_3)_{14}(O_2CCMe_3)_{12}(py)_6(H_2O)_2]$ (**2**), $[Mn_7(\mu_3\text{-}O)_3(O_3PPh)_3(O_2CCMe_3)_8(py)_3]$ (**3**), $[Mn_9Na(\mu_3\text{-}O)_4(\mu_4\text{-}O)_2(O_3PPh)_2(O_2CCMe_3)_{12}(H_2O)_2(H_2O)_{0.67}(Py)_{0.33}]$ (**4**), and $[Mn_{13}(\mu_3\text{-}O)_8(OMe)_8(O_3PPh)_4(O_2CCMe_3)_{10}]$ (**5**) are described. Complexes **4** and **5** are homovalent Mn^{III} cages, while **2** and **3** contain divalent, trivalent, and/or tetravalent ions. All the manganese centers are valence-localized, the octahedral Mn^{III} sites being recognizable by marked Jahn–Teller distortions. The magnetic properties of compounds **2**–**5** have been investigated in the polycrystalline state by magnetic susceptibility and high-field magnetization measurements, which reveal that spin ground states vary from $0 \leq S \geq 8$. AC susceptibility measurements performed on **4** and **5**, in the 1.6–10.0 K ranges show the presence of out of AC susceptibility signal (χ_M'') for **4**, and an effective energy barrier (U_{eff}) for the re-orientation of the magnetization is found to be 17 K, but for **5**, the χ_M'' maximum is found to be below 1.5 K.

Keywords: magnetic properties · manganese · mixed-valent compounds · P ligands · single-molecule magnet

Introduction

Many Mn-based clusters have been reported over the last 20 years for two main reasons: the first is biological in origin, because Mn is prominent in the active sites of metalloenzymes.[1] The most commonly studied is the water-oxidising complex (WOC) of photosystem II (PS II), the species in plants (and cyanobacteria) that brings about the oxidation of water into dioxygen. The WOC is a tetranuclear Mn cluster and therefore, numerous $\{Mn_4\}$ complexes have been synthesized as models to probe the structural changes and mechanistic processes occurring in PS II.[2] The second reason is the magnetic behavior of Mn clusters, many of which exhibit large ground spin states (S). This, coupled with a large zero-field splitting parameter (D) derived from the single-ion anisotropy of Mn^{III}, gives rise to the super paramagnetic-like property of a barrier to magnetization relaxation, which can be observed as hysteretic loops in magnetization versus field measurements.[3] Therefore these discrete molecules behave as magnets below their blocking temperatures and have been termed single-molecule magnets (SMMs).[4] Investigations have been inspired partly by the idea that SMMs could be used as molecular magnetic storage devices but also because they show unusual phenomena such as quantum-tunneling of magnetization,[5] which can be exchange-biased.[6] The last ten years has seen many attempts to produce new SMMs in the same mould as the original SMM $[Mn_{12}O_{12}(OAc)_{16}(H_2O)_4]\cdot 4H_2O\cdot 2CH_3CO_2H$,[7] and this has led to the discovery of numerous manganese SMMs ranging in nuclearity from 4 to 84.[8] The majority of

---

[a] M. Shanmugam, Dr. G. A. Timco, Prof. R. E. P. Winpenny
School of Chemistry
The University of Manchester
Oxford Road, Manchester, M13 9PL (UK)
Fax: (+44) 161-275-4616
E-mail: richard.winpenny@man.ac.uk

[b] Dr. G. Chastanet, Prof. R. Sessoli
Laboratorio di Magnetismo Molecolare
Dipartimento di Chimica
Università degli Studi di Firenze & INSTM
Via della Lastruccia n. 3, 50019 Sesto Fiorentino (Italy)

[c] Prof. T. Mallah
Laboratorie de Chimie Inorganique
UMR CNRS 8613
Université Paris Sud
91405 Orsay (France)

[d] Dr. S. J. Teat
CCLRC Daresbury Laboratory
Daresbury, Warrington, Cheshire, WA4 4AD (UK)

Table 1. Analytical data[a] for compounds **2–5**.

		C	H	N	P
2	$[Mn_{18}(\mu_3\text{-}O)_8(PhPO_3)_{14}(O_2CCMe_3)_{12}(py)_6(H_2O)_2]$	41.10 (41.58)	3.90 (4.25)	1.70 (1.67)	8.42 (8.62)
3	$[Mn_7(\mu_3\text{-}O)_3(O_3PPh)_3(O_2CCMe_3)_8(py)_3]$	45.03 (45.03)	4.72 (5.28)	2.04 (2.15)	4.78 (4.77)
4	$[Mn_9Na(\mu_3\text{-}O)_4(\mu_4\text{-}O)_2(O_3PPh)_2(O_2CCMe_3)_{12}(H_2O)_{2.66}(Py)_{0.33}]$	40.24 (39.95)	5.71 (5.70)	0.20 (0.10)	2.91 (2.80)
5	$[Mn_{13}(\mu_3\text{-}O)_8(OMe)_8(O_3PPh)_4(O_2CCMe_3)_{10}]$	34.10 (34.12)	4.61 (4.95)	–	4.99 (4.54)

[a] Calculated values are given in the parentheses.

SMMs reported to date have been clusters that contain Mn^{III} ions[9] due to pronounced magnetic anisotropy provided by the Jahn–Teller distortion. However, this presents a synthetic problem: there are few "simple" readily available sources of Mn^{III}. This has resulted in the use of two alternative techniques: 1) the use of the basic metal carboxylates of general formula, $[Mn_3O(RCO_2)_6L_3]^{0/+}$, which can contain either two or three Mn^{III} ions, and 2) the oxidation of Mn^{II} salts with permanganate (MnO_4^-). Both of these techniques have been successful, particularly the former.[10]

One route to polymetallic compounds, a route perhaps best termed "designed assembly", controls the reaction pathway by making a specific metal–ligand interaction the most significant in the system. Typical examples of this approach are the grids made by Lehn and co-workers,[11,12] the sophisticated structures made by the Saalfrank group,[13,14] or the polyhedra constructed by Fujita and co-workers based on the concept of "molecular panelling".[15] A complimentary strategy is "serendipitous assembly"[16] which produces less predictable products, but products which can be of immense interest in their own right, for example, the extraordinary polyoxomolybdate cages produced by Müller and co-workers.[17,18] Here we report some experiments in serendipitous assembly that lead to a new and diverse family of polymetallic manganese cages.

Results and Discussion

Synthesis and crystal structures: We have previously shown[19] that reaction of oxo-centered iron carboxylate triangles with phosphonates generate a series of clusters that can be regarded as being formed by the oligomerization of the triangles by bridging through the phosphonate ligands. The original aim of the synthetic program was to explore whether the same strategy could be used to assemble Mn^{n+} ions into large aggregates with new structures and magnetic properties. It was observed that the reaction proceeds well in the presence of alkali bases or amines, as these promote the reaction by deprotonation of the phosphonic acid ligands. Each component of the reaction matrix has a strong influence on the final products, and hence on the magnetic behavior. A list of the compounds presented in this report and their analytical data is given in Table 1 and full crystallographic details are presented in Table 2.

Table 2. Crystallographic data for compounds **2–5**.

	2	**3**	**4**	**5**
dimensions [mm]	0.13 × 0.04 × 0.02	0.2 × 0.1 × 0.1	0.2 × 0.2 × 0.1	0.3 × 0.3 × 0.10
system	monoclinic	monoclinic	monoclinic	monoclinic
group	$P2_1$	$C2/c$	$P2_1/n$	$C2/c$
a [Å]	15.385(2)	49.705(10)	22.427(16)	30.882(11)
b [Å]	37.468(6)	14.248(3)	19.384(14)	20.805(11)
c [Å]	21.804(3)	29.369(6)	24.660(13)	20.087(9)
β [°]	91.85(3)	115.463(4)	95.699(2)	90.373(11)
V [Å^3]	12562(3)	18778(6)	10667.5(13)	121906(10)
Z	2	8	4	4
ρ_{calcd} [g cm^{-3}]	1.377	1.406	1.473	1.419
$2\theta_{max}$	46.90	41.64	52.88	52.94
radiation	synchrotron	$Mo_{K\alpha}$	$Mo_{K\alpha}$	$Mo_{K\alpha}$
λ [Å]	0.6764	0.7107	0.7107	0.7107
T [K]	150(2)	100(2)	100(2)	100(2)
reflns	96270	31893	61775	36752
ind. reflns	42586	9833	21826	13026
reflns with $I > 2\sigma(I)$	32048	4752	11232	9125
$R1$	0.0727	0.0461	0.0515	0.0702
$wR2$	0.2174	0.0944	0.1099	0.2423

Reaction with pyridine: The reaction of $[Mn_3O(O_2CCMe_3)_6(py)_3]$ (**1**) with $PhPO_3H_2$ was investigated in the presence of pyridine as a base in acetonitrile. A brown solution of **1** in CH_3CN was stirred overnight with $PhPO_3H_2$ in the presence of pyridine in the relative ratios 1:1:1. The resultant solution was filtered before being kept for crystallization. Good single crystals grow from the filtrate in moderate yield. X-ray diffraction studies show the resulting complex to be $[Mn_{18}(\mu_3\text{-}O)_8(PhPO_3)_{14}(O_2CCMe_3)_{12}(py)_6(H_2O)_2]$ (**2**, Figure 1)

Complex **2** is a mixed-valent cage that contains sixteen Mn^{III} ions and two Mn^{IV} ions; assignment of oxidation states is confirmed by valence-bond sum analysis (Table 3) developed by Brown and Thorp and co-workers.[20] Selected bond lengths for **2** are given in Table 4.

The structure is approximately centrosymmetric, however this is not crystallographically imposed, and retains many of the oxo-centered triangles from the precursor. This is most clearly seen at the periphery of the structure where two discrete triangles are observed, which account for six of the Mn sites in **2**. The triangles in the periphery feature exclusively Mn^{III} sites around each central μ_3-oxide. Two of the

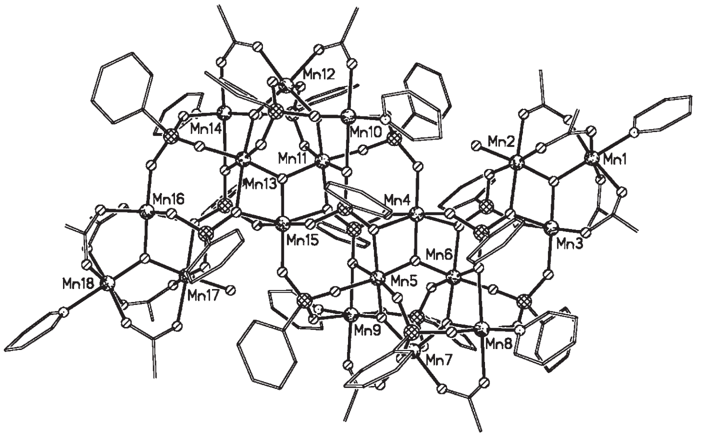

Figure 1. The structure of **2** in the crystal. Shading (for Figures 1–4): Mn atoms: heavily-shaded, random dots; P atoms: cross-hatched; O atoms: diagonal top-right bottom-left; N atoms: open; C atoms: drawn as lines.

three edges of this triangle are each bridged by two 2.11 pivalates (Harris notation[21]) groups as observed in **1**, with a terminal pyridine and a water molecule. The third edge links these triangles to the central core of the cluster.

The remaining twelve metals form two $\{Mn_6O_3\}$ fragments, each of which can be described as a triangle of vertex-sharing oxo-centered triangles. One out of six metal sites in each $\{Mn_6O_3\}$ fragment (Mn14 and Mn18 respectively) has a regular octahedral geometry (bond lengths fall within the range 1.843 to 1.977 Å), which is assigned as a tetravalent manganese site, whereas the other sites have the metals in the trivalent state. Among the three vertex-sharing triangles two of them are bridged by two phosphonates in the 3.111 coordination mode. Two more pivalates (2.11) and two terminal pyridines complete the coordination spheres of the Mn centers. The third edge of each discrete triangle (see above) is bridged to a $\{Mn_6O_3\}$ fragment by three more phosphonates and each of the phosphonates adopts three different binding modes (5.221, 4.211, and 3.111). Finally the central $\{Mn_9O_4\}$ fragments are linked to one another by four bridging phosphonates, two of which adopt the 5.221 and the other two the 3.111 mode (Figure 1).

Table 3. Bond valence sum analysis for manganese sites in **2**–**5**.

Complex	Mn site	BVS	assigned O.S	Mn site	BVS	assigned O.S	Mn site	BVS	assigned O.S
2	1	3.303	3	2	3.199	3	3	3.219	3
	4	3.221	3	5	3.115	3	6	3.255	3
	7	3.303	3	8	3.224	3	9	3.237	3
	10	3.100	3	11	3.234	3	12	3.247	3
	13	3.135	3	14	4.143	4	15	3.084	3
	16	3.165	3	17	3.064	3	18	4.051	4
3	1	3.149	3	2	1.939	2	3	3.164	3
	4	3.182	3	5	4.130	4	6	3.183	3
	7	2.104	2						
4	1	3.187	3	2	3.131	3	3	3.182	3
	4	3.242	3	5	3.136	3	6	3.197	3
	7	3.193	3	8	3.249	3	9	3.297	3
5	1	3.153	3	2	3.265	3	3	3.301	3
	4	3.255	3	5	3.224	3	6	2.814	3
	7	3.236	3						

Table 4. Selected bond lengths [Å] for **2**.

Mn1–O61	2.189(6)	Mn1–O64	2.024(5)	Mn1–O71	2.091(6)
Mn1–O73	1.861(6)	Mn2–O42	2.317(5)	Mn2–O47	1.903(5)
Mn2–O49	1.957(6)	Mn2–O61	2.235(6)	Mn2–O65	1.929(5)
Mn2–O73	1.861(6)	Mn3–O25	1.932(6)	Mn3–O33	2.215(6)
Mn3–O40	1.912(5)	Mn3–O43	1.944(6)	Mn3–O48	2.292(6)
Mn3–O68	1.867(6)	Mn4–O42	2.077(6)	Mn4–O44	1.896(6)
Mn4–O46	2.156(6)	Mn4–O56	2.045(6)	Mn4–O70	2.030(6)
Mn4–O73	1.854(5)	Mn5–O13	2.129(7)	Mn5–O45	1.937(6)
Mn5–O46	2.304(6)	Mn5–O52	1.880(6)	Mn5–O70	1.896(6)
Mn5–N4	2.061(8)	Mn6–O19	1.942(6)	Mn6–O23	2.150(7)
Mn6–O63	1.900(6)	Mn6–O66	2.205(6)	Mn6–O72	1.888(7)
Mn6–O76	1.974(7)	Mn7–O26	2.034(6)	Mn7–O30	1.895(6)
Mn7–O33	2.192(6)	Mn7–O34	1.930(6)	Mn7–O68	1.856(6)
Mn7–O74	2.122(7)	Mn8–O1	2.160(7)	Mn8–O3	1.939(6)
Mn8–O27	2.217(6)	Mn8–O32	1.910(6)	Mn8–O67	1.870(6)
Mn8–O75	1.999(6)	Mn9–O6	1.924(7)	Mn9–O8	2.197(6)
Mn9–O27	2.337(6)	Mn9–O28	1.902(6)	Mn9–O31	1.922(6)
Mn9–O67	1.887(6)	Mn10–O16	2.118(7)	Mn10–O57	1.889(6)
Mn10–O59	1.915(6)	Mn10–O64	2.433(6)	Mn10–O71	1.868(6)
Mn10–N6	2.092(8)	Mn11–O39	1.993(7)	Mn11–O41	2.166(6)
Mn11–O48	2.103(6)	Mn11–O51	1.888(6)	Mn11–O68	1.860(6)
Mn11–O69	2.047(7)	Mn12–O17	1.928(7)	Mn12–O21	2.163(6)
Mn12–O60	1.920(7)	Mn12–O62	1.897(6)	Mn12–O66	2.318(6)
Mn12–O72	1.906(6)	Mn13–O18	2.080(7)	Mn13–O20	2.078(8)
Mn13–O22	2.018(8)	Mn13–O24	2.035(8)	Mn13–O72	1.830(6)
Mn13–N5	2.055(9)	Mn14–O14	1.943(7)	Mn14–O15	1.949(7)
Mn14–O53	1.906(6)	Mn14–O55	1.901(6)	Mn14–O70	1.870(6)
Mn14–O71	1.852(6)	Mn15–O12	2.147(8)	Mn15–O36	1.909(6)
Mn15–O41	2.266(6)	Mn15–O50	1.925(6)	Mn15–O69	1.895(6)
Mn15–N3	2.067(8)	Mn16–O9	2.096(8)	Mn16–O26	2.479(6)
Mn16–O29	1.898(7)	Mn16–O37	1.889(7)	Mn16–O74	1.872(7)
Mn16–N2	2.059(8)	Mn17–O2	2.052(7)	Mn17–O4	2.066(7)
Mn17–O5	2.107(8)	Mn17–O7	2.001(7)	Mn17–O67	1.850(6)
Mn17–N1	2.066(8)	Mn18–O10	1.977(9)	Mn18–O11	1.960(8)
Mn18–O35	1.910(8)	Mn18–O38	1.902(8)	Mn18–O69	1.884(6)
Mn18–O74	1.843(7)	Mn1–O54	1.955(6)	Mn1–O58	1.893(6)

Reaction with triethylamine: If the above reaction is carried out in the presence of Et_3N but keeping all other reaction conditions identical we can make $[Mn_7(\mu_3\text{-}O)_3(O_3PPh)_3(O_2CCMe_3)_8(py)_3]$(**3**, Figure 2) in good yield (py comes from **1**), and the yield is made even better by adding 4–5 drops of pyridine. This cage contains one isolated triangle (Mn3, Mn4, Mn6), and a $\{Mn_4O_2\}$ butterfly—which can be described as two edge-sharing triangles (Mn1, Mn5, Mn7 and Mn1, Mn5, Mn2). Mn5 has a regular octahedral geometry, in which the Mn–O bonds range from 1.820 to 1.961(5) Å, and is tetravalent. Mn2 and Mn7 are also six-coordinate, but with less regular bond angles and significantly longer bonds (Mn–O 2.045–2.312(5); Mn–N 2.280 and 2.257(7) Å) and are Mn^{II} sites. Mn3 and Mn4 have a Jahn–Teller elongation typical of Mn^{III}, while Mn1 is five-coordinate with a square-pyramidal geometry with the longest bond

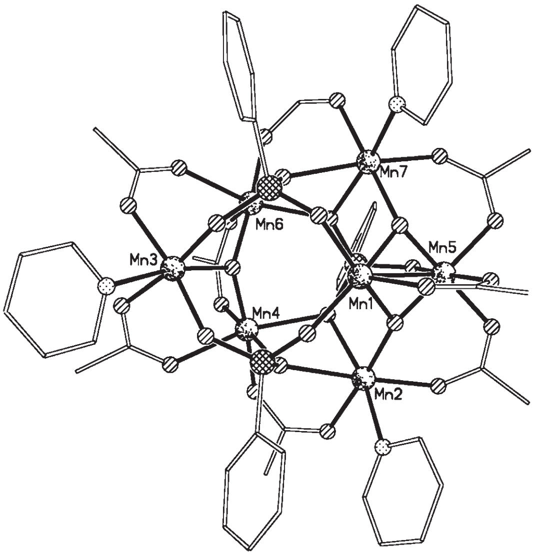

Figure 2. The structure of **3** in the crystal.

to the apex of the pyramid and this is also assigned as Mn^{III}. Mn6 has a Jahn–Teller compressed geometry, with two *trans*-Mn−O bonds of 1.828 and 1.954(5) Å, and four longer Mn−O bonds (2.017–2.123(5) Å); this is also assigned as Mn^{III}, giving a complete formula of $[Mn^{II}_2Mn^{III}_4Mn^{IV}(\mu_3\text{-}O)_3(O_3PPh)_3(O_2CCMe_3)_8(py)_3]$. Valence-bond analysis confirms this picture (see Table 3). The result is that the oxo-centred triangle is homovalent—all Mn^{III}—while the butterfly contains three different oxidation states. Selected bond lengths for **3** are given in Table 5.

Table 5. Selected bond lengths [Å] for **3**.

Mn1−O26	1.863(5)	Mn1−O27	1.868(5)	Mn1−O1	1.925(5)
Mn1−O4	1.964(5)	Mn1−O19	2.110(5)	Mn2−O23	2.090(5)
Mn2−O27	2.100(5)	Mn2−O17	2.125(5)	Mn2−O8	2.253(5)
Mn2−N2	2.280(7)	Mn2−O3	2.312(5)	Mn3−O5	1.889(5)
Mn3−O14	1.902(5)	Mn3−O2	1.918(5)	Mn3−O11	1.943(6)
Mn3−O28	2.227(5)	Mn3−N1	2.370(7)	Mn4−O28	1.856(5)
Mn4−O25	1.929(6)	Mn4−O22	1.955(5)	Mn4−O3	1.983(5)
Mn4−O8	2.196(5)	Mn4−O15	2.213(5)	Mn5−O27	1.820(5)
Mn5−O26	1.822(5)	Mn5−O9	1.929(5)	Mn5−O16	1.954(6)
Mn5−O21	1.959(5)	Mn5−O18	1.961(6)	Mn6−O28	1.828(5)
Mn6−O13	1.954(5)	Mn6−O24	2.017(6)	Mn6−O6	2.063(5)
Mn6−O10	2.091(6)	Mn6−O7	2.123(5)	Mn7−O12	2.045(6)
Mn7−O26	2.050(5)	Mn7−O20	2.117(5)	Mn7−O7	2.207(5)
Mn7−N3	2.257(7)	Mn7−O6	2.322(5)		

In the butterfly unit, the two divalent Mn sites (Mn2 and Mn7) are bridged to the tetravalent Mn site (Mn5) through two 2.11 carboxylates, and the third pivalate bridges the body of the butterfly (Mn1 and Mn5); there are also two μ_3-oxo bridges in this unit. Each of the Mn^{II} sites in the butterfly has a terminal pyridine ligand which completes the coordination sphere. Each edge of the isolated triangle (Mn3, Mn4, and Mn6) is bridged differently: one edge by two pivalates, another by only one pivalate group, and the third edge is connected to the butterfly unit through three phosphonates, with two of them showing the 4.211 and the other one the 3.111 mode. Two more pivalate groups link the triangle and butterfly.

Reaction with sodium methoxide: If we use sodium methoxide as a base we generate $[Mn_9Na(\mu_3\text{-}O)_4(\mu_4\text{-}O)_2(O_3PPh)_2(O_2CCMe_3)_{12}(H_2O)_2(H_2O)_{0.67}(py)_{0.33}]$ (**4**, Figure 3) in a low but reproducible yield of about 4 %. Compound **4** can be described based on a central Mn site (Mn2) that is bound to four μ_3-oxides, which form bridges to six Mn sites (Mn5, Mn3, Mn6, Mn7, Mn9, Mn8); Mn2 is therefore a vertex of four oxo-centered triangles, while Mn5 and Mn7 are shared between two of these triangles (Figure 3). The final two μ_3-oxides attach the final two Mn sites to this heptametallic core, creating two further triangles (Mn3, Mn6, Mn4 and Mn8, Mn9, Mn1). For charge balance a sodium ion sits on the cage, bridged to five manganese sites (Mn2, Mn3, Mn5, Mn6, Mn7) through two μ_4-oxo bridges and two carboxylate groups (3.11). This sodium ion is six-coordinate; two water molecules complete the coordination sphere. The core is related to previous nonanuclear carboxylate cages $[Mn_9O_7(O_2CPh)_{13}(py)_2]$,[22] $[Na_2Mn_9O_7(O_2CPh)_{15}(MeCN)_2]$,[23] and $[K_2Mn_9O_7(O_2CCMe_3)_{15}(HO_2CCMe_3)_2]$.[24]

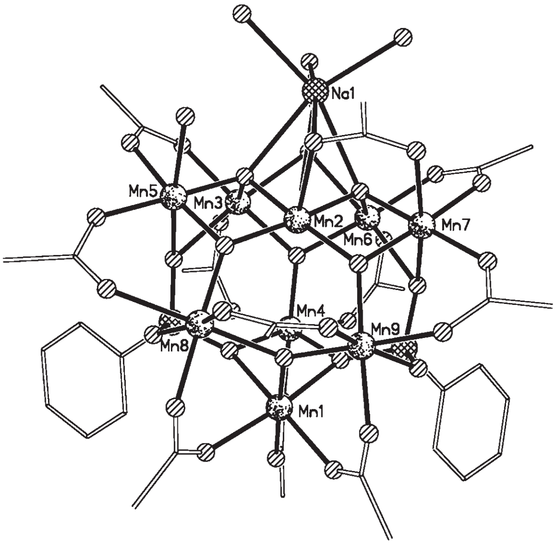

Figure 3. The structure of **4** in the crystal. Shading: Na atom: cross-hatched and labeled.

We have described such cages as fragments of an icosahedron[24] and that description is valid here. Eight of the Mn sites (all except Mn2), the two P atoms, and a sodium atom lie at the vertices of a distorted icosahedron that is missing one vertex which would complete the pentagonal ring of Mn3, Mn5, Mn6, and Mn7 (see Figure 3). While Mn2 may appear to be in this ring, it does not lie on the surface of an icosahedron but lies near the center of the polyhedron. The two phosphonates both adopt the 5.221 binding mode, which allows them to occupy vertices of an icosahedron, while the carboxylates that bridge the Mn sites together in the periphery of the distorted icosahedra adopt the 2.11

Table 6. Selected bond lengths [Å] for **4**.

Mn1−O36	1.810(3)	Mn1−O15	1.958(3)	Mn1−O2	2.007(3)
Mn1−O9	2.077(3)	Mn1−O33	2.100(3)	Mn1−O30	2.169(3)
Mn2−O38	1.873(3)	Mn2−O34	1.893(3)	Mn2−O37	1.912(3)
Mn2−O35	1.912(3)	Mn2−O19	2.195(3)	Mn3−O34	1.916(3)
Mn3−O39	1.919(3)	Mn3−O6	1.940(3)	Mn3−O7	1.949(3)
Mn3−O32	2.229(3)	Mn4−O39	1.878(3)	Mn4−O16	1.930(3)
Mn4−O30	1.990(3)	Mn4−O5	2.008(3)	Mn4−O11	2.069(3)
Mn4−O33	2.112(3)	Mn5−O37	1.880(3)	Mn5−O34	1.901(3)
Mn5−O22	1.905(3)	Mn5−O8	1.957(3)	Mn5−O27	2.302(5)
Mn5−O32	2.310(3)	Mn5−N1	2.317(9)	Mn6−O35	1.885(3)
Mn6−O39	1.923(3)	Mn6−O12	1.936(3)	Mn6−O17	1.948(3)
Mn6−O29	2.188(3)	Mn6−O23	2.264(3)	Mn7−O38	1.870(3)
Mn7−O35	1.899(3)	Mn7−O14	1.927(3)	Mn7−O18	1.953(3)
Mn7−O20	2.223(3)	Mn7−O29	2.342(3)	Mn8−O37	1.897(3)
Mn8−O10	1.925(3)	Mn8−O31	1.942(3)	Mn8−O4	1.943(3)
Mn8−O36	2.138(3)	Mn8−O21	2.231(3)	Mn9−O36	1.887(3)
Mn9−O38	1.893(3)	Mn9−O1	1.955(3)	Mn9−O13	1.965(3)
Mn9−O3	2.137(4)	Mn9−O28	2.159(3)	Na1−O24	2.287(4)
Na1−O26	2.337(5)	Na1−O25	2.482(5)	Na1−O35	2.536(4)
Na1−O34	2.563(4)	Na1−O23	3.018(4)		

mode. All the manganese ions show a Jahn–Teller elongation as expected for Mn^{III}. Selected bond lengths for **4** are given in Table 6.

Reaction with sodium hydroxide: Using NaOH in MeOH gives a tridecametallic cluster, $[Mn_{13}(\mu_3\text{-}O)_8(OMe)_8(O_3PPh)_4(O_2CCMe_3)_{10}]$ (**5**, Figure 4a), in 60% yield. The structure features two trigonal prisms, rotated at 90° with respect to one another, with each triangular face of the prism formed from an oxo-centered triangle (see Figure 4b). For each prism two square faces are occupied by 4.211 bridging phosphonates. The third square face is used to link the two prisms; each triangle unit in the trigonal prism exhibits the same bridging through carboxylates in that two edges of the each triangle are bridged by a single pivalate (2.11) and the third edge connected by a methoxide group. This accounts for four of the methoxide groups out of eight. The link between the triangles which forms the trigonal prism is provided by a third pivalate group (2.11). The other four methoxide groups connect the two orthogonal trigonal prisms. The thirteenth Mn center lies between the two square faces and is bound to four μ_3-oxides; each oxide then binds to two further Mn centers, one derived from each of the trigonal prisms. In related Fe^{III} chemistry we have reported the isolated trigonal prism, which has the identical bridging found in **5** save that the final square face is occupied by a 4.22 bridging peroxide.[19]

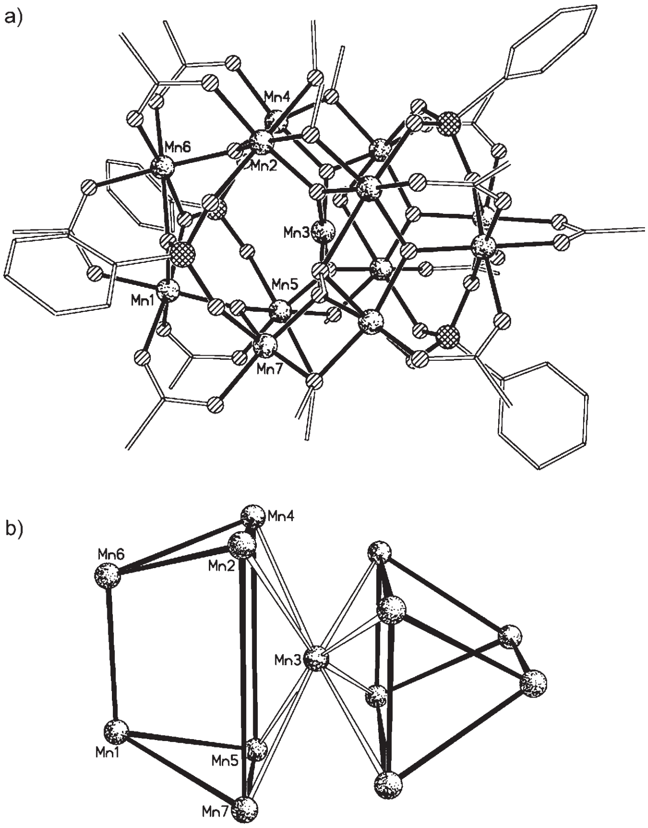

Figure 4. a) The structure of **5** in the crystal. b) Orthogonal trigonal prism view of **5** metal core.

The central Mn site [Mn3] has a square-planar geometry, with Mn−O bonds of 1.822–1.847(4) Å. This is unusual for manganese in any oxidation state.[25] Given the electronic structure, this is most plausibly assigned as Mn^{III}. The remaining twelve sites are also Mn^{III}, based on geometries that show Jahn–Teller distortions; compressions for Mn1 and Mn6 and elongations for the other Mn sites. This analysis, combined with the crystal structure creates the problem that the charge does not balance: **5** would be a tri-anion and there are no cations in the lattice. While the oxides, phosphonates, and pivalates are clearly deprotonated, four of the bridging "methoxides" have short intramolecular O···O contacts (O···O ca. 2.9 Å) to O atoms from phosphonates. It is possible these contacts reflect MeO−H···O(phosphonate) hydrogen bonds, which would allow the charge to be balanced. Selected bond lengths of **5** are given in Table 7.

Magnetic susceptibility studies: Direct current magnetic susceptibility studies were performed on polycrystalline powder samples of **2**–**5** in the 1.5–300 K range at an applied field of 0.1 T. The size of the clusters and their low symme-

Table 7. Selected bond lengths [Å] for **5**.

Mn1−O24#1	1.853(3)	Mn1−O12	1.937(4)	Mn1−O16#1	2.053(5)
Mn1−O14#1	2.057(6)	Mn1−O1	2.081(4)	Mn1−O5	2.088(4)
Mn2−O22	1.849(3)	Mn2−O25	1.904(4)	Mn2−O9	1.928(4)
Mn2−O19	1.962(4)	Mn2−O4	2.127(4)	Mn2−O17	2.397(4)
Mn3−O22#1	1.830(3)	Mn3−O22	1.830(3)	Mn3−O23	1.833(5)
Mn3−O26	1.844(5)	Mn4−O23	1.853(3)	Mn4−O25	1.907(4)
Mn4−O7	1.922(4)	Mn4−O21	1.947(3)	Mn4−O2	2.140(4)
Mn4−O17	2.419(4)	Mn5−O26	1.847(3)	Mn5−O15	1.909(4)
Mn5−O24	1.929(4)	Mn5−O20	1.967(4)	Mn5−O6#1	2.164(5)
Mn5−O18	2.365(4)	Mn6−O25	1.907(3)	Mn6−O11	1.993(4)
Mn6−O10	2.079(5)	Mn6−O1	2.107(4)	Mn6−O5	2.128(4)
Mn6−O8	2.130(5)	Mn7−O22	1.855(3)	Mn7−O13	1.908(4)
Mn7−O24	1.938(4)	Mn7−O19	1.952(4)	Mn7−O3#1	2.128(4)
Mn7−O18	2.408(4)	O23−Mn4#1	1.853(3)	O24−Mn1#1	1.853(3)
O26−Mn5#1	1.847(3)	O3−Mn7#1	2.128(4)	O6−Mn5#1	2.164(5)
O14−Mn1#1	2.057(6)	O16−Mn1#1	2.053(5)	O20−Mn5#1	1.967(4)
O21−Mn4#1	1.947(3)				

try prevents us from modeling their variable-temperature magnetic behavior.

A plot of the product of the molar magnetic susceptibility (χ_M) and temperature versus temperature of complex **2** is shown in Figure 5a. Complex **2** has a $\chi_M T$ value of 47.8 $cm^3 K mol^{-1}$ at room temperature, which is smaller than the value calculated for 16 Mn^{III} and two Mn^{IV} (calculated value for $g=2.00$ is 51.75 $cm^3 K mol^{-1}$). The $\chi_M T$ value slowly increases as the temperature decreases and reaches a maximum value of 53.6 $cm^3 K mol^{-1}$ at 49 K. To determine the exact ground state of complex **2**, variable-field dc magnetization data were collected at applied fields of 0.0 to 12.0 T at 1.5 K. In contrast to the maximum $\chi_M T$ value, the M versus H plot shows (Figure 5b) a step at around 3 μ_B, and the magnetic moment continuously increases with increasing field. For such a high nuclearity cluster, we have a dense population of excited states of varying spin within a small energy gap to that of ground state, such problems have been previously discussed by Christou and co-workers.[9a] The ground spin state of complex **2** is probably small or may be a diamagnetic ground state in zero-field, which causes the small gradient in M versus H at low fields. As the field increases higher spin excited states become populated leading to a more rapid increase in M. The observed maximum $\chi_M T$ value is therefore due to an average value of all the populated excited high spin state levels at the field and temperature measured. We have recently shown a more well-defined step in a {Mn_{20}} cage with a spin ground state of 20 which becomes $S=30$ at high field.[11] The size of the cluster prevents any attempt to fit the magnetic data to a spin Hamiltonian.

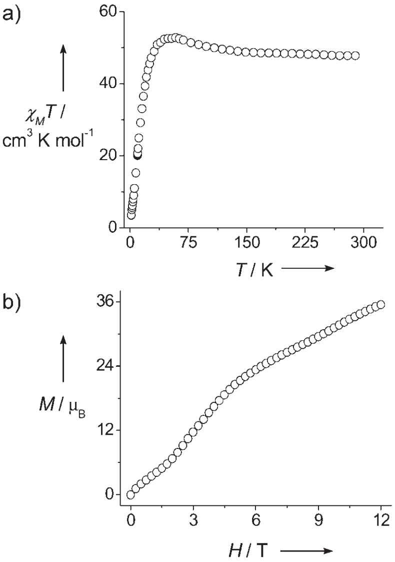

Figure 5. a) Temperature dependence of $\chi_M T$ for a polycrystalline sample of **2**, b) magnetization versus field data for **2**.

Figure 6a shows the $\chi_M T$ versus T plot for **3**. $\chi_M T$ has a value of 17.5 $cm^3 K mol^{-1}$ at 300 K which is significantly smaller than the spin-only value of 22.65 $cm^3 K mol^{-1}$ ($g=2.00$) expected for four Mn^{III}, two Mn^{II}, and one Mn^{IV} uncorrelated spins. This room-temperature $\chi_M T$ value suggests the presence of strong antiferromagnetic exchange within the cluster—probably between Mn^{III} and Mn^{IV} centers. $\chi_M T$ starts to increase slightly upon decreasing the temperature and reaches a maximum value of 23.0 $cm^3 K mol^{-1}$ at 6.0 K, which is consistent with an $S=13/2$ ground state. Magnetization data measured at 2, 3, and 4 K (Figure 6b) confirms this picture, showing a sharp increase in the magnetization followed by pronounced saturation around 13 μ_B upon increasing the applied field. The magnetization can be fitted using the parameters $S=13/2$, $D=0.18$ cm^{-1}, $E/D=0.31$, $g=1.97$. The fit neglects population of excited states of higher spin as the field increases but the resulting parameters are not unreasonable.

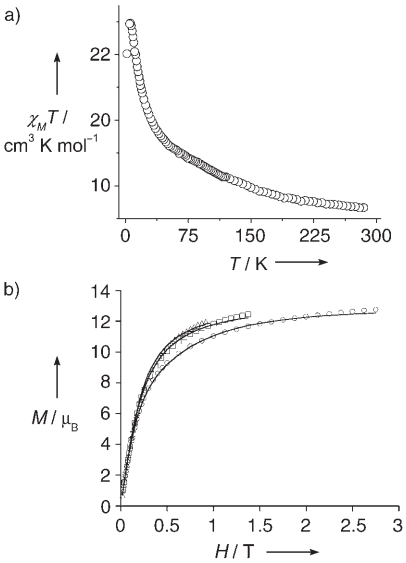

Figure 6. a) Temperature dependence of $\chi_M T$ for a polycrystalline sample of **3**, b) magnetization versus field data for **3** (△ = 2 K, □ = 3 K, ○ = 4 K). The solid line is a fit of this data using parameters in the text.

The magnetic susceptibilities of **2** and **3** were measured in zero applied field down to temperatures as low as 1.4 K by the use of an AC susceptometer. In both cases, paramagnetic behavior, with no imaginary component of the a.c susceptibility was observed.

Magnetic susceptibility measurements on a powder sample of **4** are illustrated in Figure 7a as a $\chi_M T$ versus T plot. The $\chi_M T$ value begins at 300 K, 21.9 $cm^3 K mol^{-1}$ which is below the expected spin-only value (27.00 $cm^3 K mol^{-1}$ for $g=2.00$) for nine trivalent Mn centers. This shows that intramolecular antiferromagnetic exchange is significant. $\chi_M T$ remains constant until 88 K, where it begins to increase to a maximum value of approximately 34 $cm^3 K mol^{-1}$ at 5.7 K, before dropping sharply below this temperature. The maximum in $\chi_M T$ suggests a high-spin ground state, with the low temperature decrease assigned to zero-field splitting, Zeeman effects, and/or intermolecular antiferromagnetic interactions. To determine the spin ground state for **4** magneti-

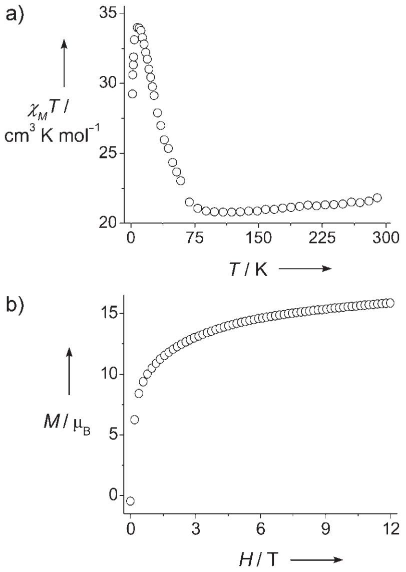

Figure 7. a) Temperature dependence of $\chi_M T$ product for a polycrystalline sample of **4**, b) magnetization versus field data for **4**.

zation data were collected in the ranges of 0.0–12.0 T at 1.5 K, and these are plotted as magnetization (M) against field (H) in Figure 7b. The magnetization curve increases rapidly at low field and reaches a plateau at higher fields, with a saturation value of 15.8 μ_B. By using the simple relation $M_{sat}/N\mu_B = gS$, and assuming $g = 2.0$, a ground state of $S = 8$ can be proposed for **4**.

A series of a.c. susceptibility studies were undertaken to see if **4** acts as a single-molecule magnet. When the rate at which the magnetization of a molecule relaxes is close to that of an applied a.c. field, an out-of-phase a.c. susceptibility signal (χ_M'') will be observed, in conjunction with a concomitant decrease in the in-phase susceptibility (χ'_M/T); essentially at low temperature, where thermal energy is not sufficient to overcome the barrier for relaxation, the magnetization of the molecule cannot change direction as quickly as the change in the oscillating field. At the temperature where χ''_M is a maximum, the relaxation rate ($1/\tau$) equals the a.c. angular frequency ($\omega = 2\pi\gamma$), and thus the measurement of peak maxima at several different frequencies provides lnK versus $1/T$ data (since $1/\tau = K$) and the barrier to relaxation can then be estimated from the Arrhenius equation. A series of a.c. susceptibility studies were carried out in the 1.5–10.0 K range in a 8×10^{-5} T field oscillating at frequencies up to 20 kHz. The in-phase (χ'_M versus T) and out-of-phase (χ''_M versus T) signals for **4** are shown in Figure 8. There is a frequency-dependent decrease in the χ'_M/T signal, and a frequency-dependent out-of-phase signal at $T \leq 2.5$ K. Both are strong indicators of SMM behavior. The data obtained were fit to the Arrhenius equation (see inset of Figure 8) to give an effective energy barrier for the reorientation of the magnetization U_{eff} of 17.7 K. The derived zero-field splitting parameter (D) for this system from its barrier is 0.27 K, since $D = U_{eff}/S^2$ for an integer spin system.

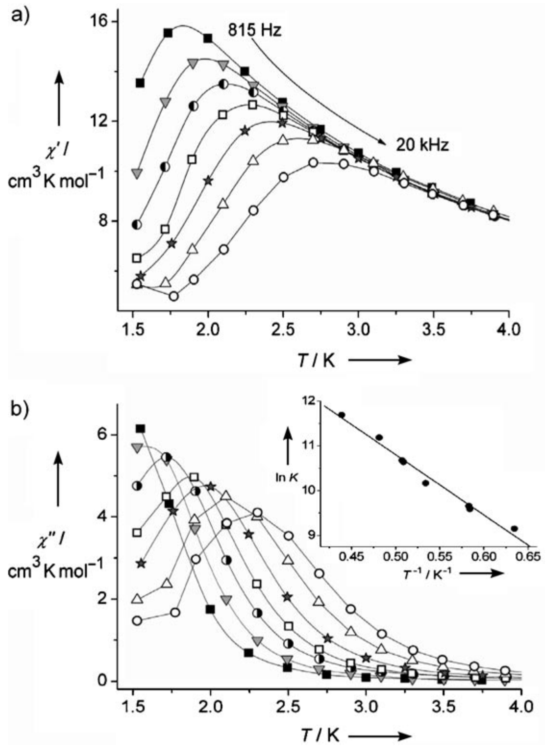

Figure 8. χ'_M (top) and χ''_M (bottom) versus T for complex **4** measured by a.c. susceptibility with frequency ranging from 815 Hz to 25 kHz in logarithmic spacing. Inset: temperature dependence of the relaxation time plot of **4**.

Figure 9a is the $\chi_M T$ versus T plot for **5**. At 300 K the observed value of $\chi_M T$, 28.3 cm^3 K mol^{-1} is lower than that of value expected for spin only uncorrelated metals centers (39.0 cm^3 K mol^{-1} for $g = 2.00$). $\chi_M T$ gradually decreases with decreasing temperature to a plateau value of

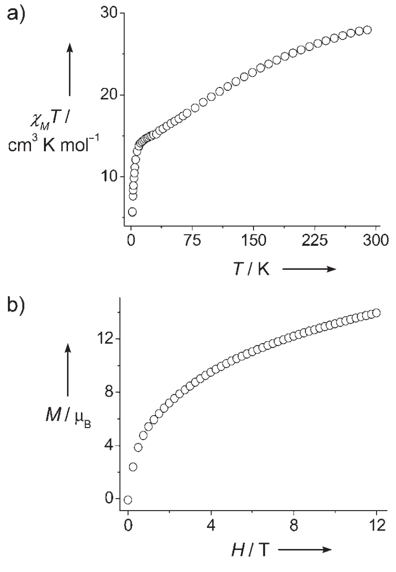

Figure 9. a) Temperature dependence of $\chi_M T$ for a polycrystalline sample of **5**, b) magnetization versus field data for **5**.

14.8 $cm^3 K mol^{-1}$ at 13 K then sharply falls below this temperature. These d.c. data are thus consistent with a predominantly antiferromagnetic interaction between the metal centers, but with a relatively large spin ground state causing the plateau. The value of $\chi_M T$ at this plateau is consistent with a ground state of $S=5$. Magnetization measurements performed on **5** are shown in Figure 9b. There is a rapid increase in the magnetization at low field and magnetic moment then continues to increase and has not saturated at the highest field measured. A possible explanation is that there are low-lying excited states of higher spin and that these become populated at higher field, hence preventing saturation.

The dynamic magnetic susceptibility of complex **5** at very low temperature is shown in Figure 10. The real component (χ'_M) increases on lowering the temperature, as expected for a paramagnet, down to about 3 K. Below this temperature the rise in the χ'_M curve depends on the frequency of the oscillating field. Similarly for the imaginary component (χ''_M), we observe frequency-dependent behavior and a rise in χ''_M, however a maximum is not observed above 1.5 K. The behavior suggests that **5** may be a SMM, but one with a very small energy barrier for reorientation of magnetization. Studies at even lower temperature would be required to prove this assertion.

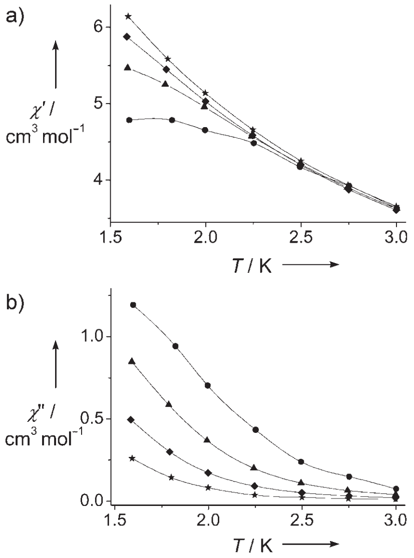

Figure 10. χ'_M (top) and χ''_M (bottom) versus T for complex **5** measured by a.c. susceptibility with frequency ranging from 910 Hz to 25 kHz in logarithmic spacing.

Conclusion

Complexes **2**–**5** were all made from similar reactions and the identity of the cluster isolated is controlled by the nature of the base used. The complexes exhibit a range of magnetic behavior: **2** and **3** possess a small and a moderate spin ground state, respectively. For **3** we have fitted magnetization data with a positive D value, which is consistent with the absence of any features in χ'' as measured by ac susceptibility. Compound **4** is an SMM with a measurable energy barrier, whereas **5** may be an SMM but with a very small barrier. This study confirms that nuclearity plays a minor role in the dynamics of the magnetization and that optimization of the ground spin state and anisotropy remains the key point to observe SMM behavior.

This work demonstrates the versatile bridging potential of the phosphonate ligands for the assembly of Mn^{n+} ions into aggregates. The precursor $\{Mn_3\}$ triangles can be recognized in all the resulting cages (Figure 11). In **2**, **3**, and **5**, triangles are found bridged to other fragments through phosphonates. We also find condensed triangles that are formed by two distinct processes. In **2**, the condensation is vertex-sharing, to produce $\{M_6O_3\}$ triangles at the center of the cage. In **3** and **4**, $\{M_4O_2\}$ “butterflies” are found; in **4** some of the vertices of the butterflies are shared with additional triangles. At present we cannot predict or control how the phosphonates assemble the pre-formed metal clusters into larger clusters, but it is clear that this is a useful strategy for making bigger polymetallic compounds.

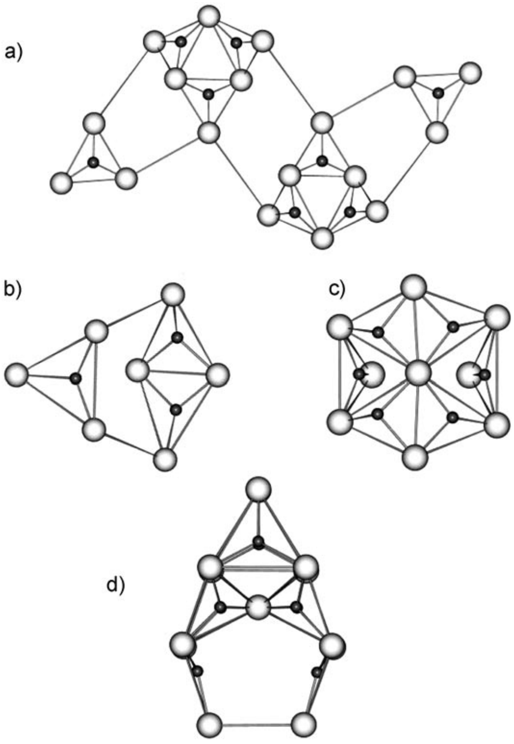

Figure 11. Schematic representation of the structures of: a) **2**, b) **3**, c) **4**, and d) **5**, showing how the complexes are constructed from oxo-centered Mn triangles.

Experimental Section

$[Mn_3O(O_2CCMe_3)_6(py)_3]$ 1: Compound **1** was made by a literature method.[26]

Compound 2: Compound **1** (0.57 g, 0.56 mmol) and $PhPO_3H_2$ (0.09 g, 0.56 mmol) were dissolved in MeCN (10 mL) and pyridine (0.05 mL) was added. The reaction mixture was stirred for 12 h, filtered, and the filtrate was allowed to stand at room temperature. Crystals of **2** formed after two days. Yield based on metal: 0.20 g (43 %).

Compound 3: As for **2**, but replacing pyridine with NEt_3 (0.14 mL) and the solution was stirred for 30 min. Yield based on metal: 0.32 g (68 %).

Compound 4: As for **2**, but replacing pyridine with NaOMe (0.04 g). The crystals were formed from the filtrate over two weeks. Yield based on metal: 0.02 g (4 %).

Compound 5: Compound **1** (0.57 g, 0.56 mmol) and $Na_2(O_3PPh)$ (0.11 g, 0.56 mmol) were mixed in MeOH (10 mL), and NaOH (0.24 g, 6 mmol) in H_2O (0.5 mL) was added. The solution was stirred overnight and filtered. Crystals of **5** grew from the filtrate after 10 days. Yield based on metal: 0.21 g (60 %).

X-ray studies: Data were collected on Bruker SMART CCD diffractometer ($Mo_{K\alpha}$, $\lambda = 0.71073$ Å except **2** where $\lambda = 0.6892$ Å). In all cases the selected crystals were mounted on the tip of a glass pin using Paratone-N oil and placed in the cold flow produced with an Oxford Cryocooling device. Complete hemispheres of data were collected by using ω-scans (0.3°, 30 s per frame). Integrated intensities were obtained with SAINT+ [27] and they were corrected for absorption using SADABS.[27] Structure solution and refinement was performed with the SHELX-package.[27] The structures were solved by direct methods and completed by iterative cycles of ΔF syntheses and full-matrix least-squares refinement against F.

CCDC-279721–CCDC-279724 contain the supplementary crystallographic data for this paper. These data can be obtained free of charge from the Cambridge Crystallographic Data Centre via www.ccdc.cam.ac.uk/data_request/dif.

Magnetic measurements: The magnetic properties of polycrystalline samples were investigated by using a Cryogenic M600 SQUID magnetometer and a home-developed ac probe based on the Oxford Inst. MAGLAB platform.[28]

Acknowledgements

This work was supported by the EC-TMR Network “QuEMolNa” (MRTN-CT-2003–504880), the EC NE “MAGMANet” and an ORS award to M.S. and the University of Manchester. M. S. thanks EST, FP6–504204: MOLMAG for supporting a study period in Florence.

---

[1] *Manganese Redox Enzymes* (Ed.: V. L. Pecoraro), VCH, Weinheim, **1992**.

[2] a) K. N. Ferreira, T. M. Iverson, K. Maghlaoui, J. Barber, S. Iwata, *Science* **2004**, *303*, 1831–1838; b) A. Mishra, W. Wernsdorfer, K. A. Abboud, G. Christou, *Chem. Commun.* **2005**, *1*, 54–56.

[3] a) E. K. Brechin, M. Soler, G. Christou, J. Davidson, D. N. Hendrickson, S. Parsons, W. Wernsdorfer, *Polyhedron* **2003**, *22*, 1771–1775; b) E. K. Brechin, M. Soler, G. Christou, M. Helliwell, S. J. Teat, W. Wernsdorfer, *Chem. Commun.* **2003**, *11*, 1276–1277.

[4] R. Sessoli, D. Gatteschi, D. N. Hendrickson, G. Christou, *MRS Bull.* **2000**, *25*, 66–71.

[5] a) J. R. Friedman, M. P. Sarachik, J. Tejada, R. Ziolo, *Phys. Rev. Lett.* **1996**, *76*, 3830–3833; b) L. Thomas, F. Lionti, R. Ballou, D. Gatteschi, R. Sessoli, B. Barbara, *Nature* **1996**, *383*, 145–147.

[6] W. Wernsdorfer, N. Aliaga-Acaldse, D. N. Hendrickson, G. Christou, *Nature* **2002**, *416*, 406–409.

[7] a) R. Sessoli, H.-L. Tsai, A. R. Schake, S. Wang, J. B. Vincent, K. Folting, D. Gatteschi, G. Christou, D. N. Hendrickson, *J. Am. Chem. Soc.* **1993**, *115*, 1804–1816; b) R. Sessoli, D. Gatteschi, A. Caneschi, M. A. Novak, *Nature* **1993**, *365*, 141–143.

[8] a) M. Soler, W. Wernsdorfer, K. Folting, M. Pink, G. Christou, *J. Am. Chem. Soc.* **2004**, *126*, 2156–2165, and references therein; b) A. J. Tasiopolous, A. Vinslava, W. Wernsdorfer, K. A. Abboud, G. Christou, *Angew. Chem.* **2004**, *116*, 2169–2173; *Angew. Chem. Int. Ed.* **2004**, *43*, 2117–2121.

[9] D. N. Hendrickson, G. Christou, H. Ishimoto, J. Yoo, E. K. Brechin, A. Yamaguchi, E. M. Rumberger, S. M. J. Aubin, Z. Sun, G. Aromz, *Polyhedron* **2001**, *20*, 1479–1488.

[10] S. Maheswaran, G. Chastanet, S. J. Teat, T. Mallah, R. Sessoli, W. Wernsdorfer, R. E. P. Winpenny, *Angew. Chem.* **2005**, *117*, 2484–2491; *Angew. Chem. Int. Ed.* **2005**, *44*, 5044–5048.

[11] J. Rojo, F. J. Romero-Salguero, J. M. Lehn, G. Baum, D. Fenske, *Eur. J. Inorg. Chem.* **1999**, 1421–1428.

[12] E. Breuning, U. Ziener, J. M. Lehn, E. Wegelius, K. Rissanen, *Eur. J. Inorg. Chem.* **2001**, 1515–1521.

[13] R. W. Saalfrank, U. Reimann, M. Goritz, F. Hampel, A. Scheurer, F. W. Heinemann, M. Buschel, J. Daub, V. Schunemann, A. X. Trautwein, *Chem. Eur. J.* **2002**, *8*, 3614–3619.

[14] R. W. Saalfrank, H. Glaser, B. Demleitner, F. Hampel, M. M. Chowdhry, V. Schunemann, A. X. Trautwein, G. B. M. Vaughan, R. Yeh, A. V. Davis, K. N. Raymond, *Chem. Eur. J.* **2002**, *8*, 493–497.

[15] M. Fujita, K. Umemoto, M. Yoshizawa, N. Fujita, T. Kusukawa, K. Biradha, *Chem. Commun.* **2001**, 509–518.

[16] R. E. P. Winpenny, *J. Chem. Soc. Dalton Trans.* **2002**, 1–10.

[17] A. Müller, P. Kögerler, *Coord. Chem. Rev.* **1999**, *182*, 3–17.

[18] A. Müller, P. Kögerler, A. W. M. Dress, *Coord. Chem. Rev.* **2001**, *222*, 193–218.

[19] E. I. Tolis, M. Helliwell, S. Langley, J. Raftery, R. E. P. Winpenny, *Angew. Chem.* **2003**, *115*, 3934–3938; *Angew. Chem. Int. Ed.* **2003**, *42*, 3804–3808.

[20] a) I. D. Brown, K. K. Wu, *Acta Crystallogr. Sect. B* **1976**, *32*, 1957–1959; b) W. Liu, H. H. Thorp, *Inorg. Chem.* **1993**, *32*, 4102–4105.

[21] Harris notation describes the binding mode as [X.Y1Y2Y3···Y*n*], where X is the overall number of metals bound by the whole ligand, and each value of Y refers to the number of metal atoms attached to the different donor atoms. See: R. A. Coxall, S. G. Harris, D. K. Henderson, S. Parsons, P. A. Tasker, R. E. P. Winpenny, *J. Chem. Soc. Dalton Trans.* **2000**, 2349–2356.

[22] D. W. Low, D. M. Eichhorn, A. Dragnescu, W. H. Armstrong, *Inorg. Chem.* **1991**, *30*, 877–878.

[23] S. Wang, J. C. Huffman, K. Folting, W. E. Streib, E. B. Lobkovsky, G. Christou, *Angew. Chem.* **1991**, *103*, 1657–1659; *Angew. Chem. Int. Ed. Engl.* **1991**, *30*, 1672–1674.

[24] M. Murrie, S. Parsons, R. E. P. Winpenny, *J. Chem. Soc. Dalton Trans.* **1998**, 1423–1424.

[25] B. D. Murray, P. P. Power, *J. Am. Chem. Soc.* **1984**, *106*, 7011–7015.

[26] R. Wu, M. Poyraz, F. E. Sowrey, C. E. Anson, S. Wocadlo, A. K. Powell, U. A. Jayasooriya, R. D. Cannon, T. Nakamoto, M. Katada, H Sano, *Inorg. Chem.* **1998**, *37*, 1913–1921.

[27] SHELX-PC Package, Bruker Analytical X-ray Systems, Madison, WI, **1998**.

[28] S. Midollini, A. Orlandini, P. Rosa, L. Sorace, *Inorg. Chem.* **2005**, *44*, 2060–2066.

Received: February 3, 2006
Revised: May 31, 2006